Solar-Driven Photocatalytic N_2 Reduction to Ammonia Using Plasmonic Au@NiZIF-8 MOF Hybrids

Belén Arjones-Fernández, Ankur Malik, Lucía Guillade, Rudranarayan Khatua, Lucas V. Besteiro, Ana Sousa-Castillo, Margarita Vázquez-González,* Ramón A. Álvarez-Puebla,* and Miguel A. Correa-Duarte**

Photocatalytic ammonia synthesis has emerged as a sustainable alternative to the fossil-fuel-dependent industrial Haber-Bosch process, utilizing solar energy to convert atmospheric nitrogen and water into NH_3 under mild conditions. While this method significantly reduces CO_2 emissions, it faces challenges such as low nitrogen solubility in water and competition with the hydrogen evolution reaction, which hinder its efficiency and scalability. Here, a core-shell approach is employed to incorporate controlled-morphology plasmonic gold nanoparticles (AuNPs) into Ni-doped ZIF-8 metal-organic frameworks (MOF_S), forming a hybrid photocatalyst. In this design, AuNPs serve as the core, while the NiZIF-8 shell prevents nanoparticle agglomeration and facilitates enhanced nitrogen and proton transport to the AuNP surface during illumination. The Au@NiZIF-8 photocatalyst outperforms NiZIF-8 alone, benefiting from improved electron transfer, energy migration, and localized field polarization. These synergistic effects enhance nitrogen activation and stabilize reaction intermediates, significantly improving catalytic efficiency and selectivity. Furthermore, the catalytic activity remains stable across three consecutive cycles.

1. Introduction

Ammonia (NH_3) is an essential raw material, primarily used in fertilizers, plastics, and explosives.[1–3] Since its development in 1909, the Haber-Bosch process has been the dominant production method, yielding ≈150 million metric tons annually with an expected growth of 2–3% per year due to rising global demand.[4,5] Despite its exothermic nature ($N_2(g) + 3H_2(g) \rightarrow 2NH_3(g)$), the reaction does not proceed efficiently under mild conditions. The high dissociation energy of the N≡N bond requires extreme temperatures (300 – 600°C) and pressures (150 – 300 atm), making the process energy-intensive. The Haber–Bosch process consumes 1 – 2% of global energy production and relies on hydrogen derived from fossil fuels, accounting for ≈50% of worldwide H_2 consumption.[6] This results in significant CO_2 emissions, ≈2 tons per ton of NH_3 produced, contributing 3% of global greenhouse gas emissions.[7] In contrast, nitrogenase enzymes in nature synthesize NH_3 from N_2 under ambient conditions using energy from photosynthesis, but their output is insufficient for industrial needs.[8] Efforts to decarbonize ammonia production include green hydrogen (from water electrolysis), electrochemical synthesis, and biomimetic catalysts that mimic nitrogenase. However, scalability and cost remain key challenges in replacing the century-old Haber-Bosch method.

Solar energy is among the most abundant energy sources on Earth, and leveraging photocatalytic technology to convert it into chemical energy offers a promising pathway to address energy shortages and environmental challenges.[9] Photocatalytic ammonia synthesis offers a sustainable alternative to the

---

B. Arjones-Fernández, A. Malik, L. Guillade, R. Khatua, L. V. Besteiro,
A. Sousa-Castillo, M. Vázquez-González, M. A. Correa-Duarte
CINBIO, Universidade de Vigo
Vigo 36310, Spain
E-mail: ana.sousa@uvigo.es; margarita.vazquez@uvigo.es;
macorrea@uvigo.es

R. A. Álvarez-Puebla
Department of Physical and Inorganic Chemistry
Universitat Rovira i Virgili
Tarragona 43007, Spain
E-mail: ramon.alvarez@urv.cat

R. A. Álvarez-Puebla
ICREA—Institució Catalana de Recerca i Estudis Avançats
Barcelona 08010, Spain

M. A. Correa-Duarte
Southern Galicia Institute of Health Research (IISGS)
Vigo 36310, Spain

M. A. Correa-Duarte
Biomedical Research Networking Center for Mental Health (CIBERSAM)
Vigo 36310, Spain

The ORCID identification number(s) for the author(s) of this article can be found under https://doi.org/10.1002/adom.202502759

DOI: 10.1002/adom.202502759

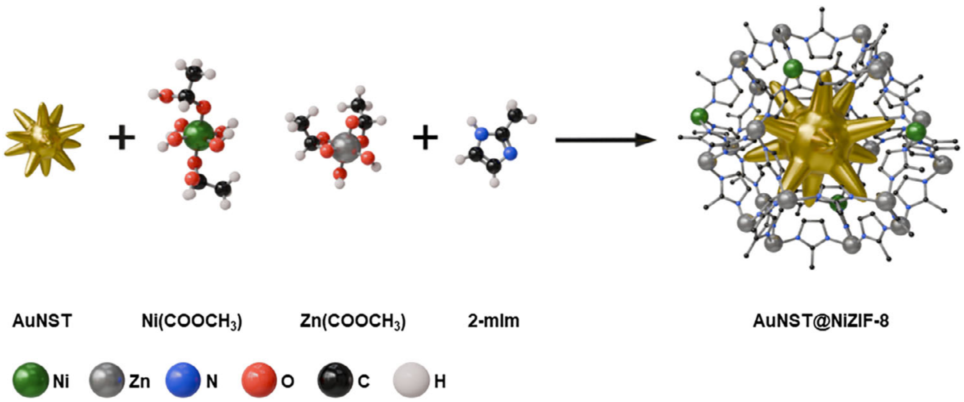

Figure 1. Schematic illustration of the synthetic process for the AuNST@NiZIF-8 hybrid.

energy-intensive Haber–Bosch process by utilizing solar energy to convert atmospheric nitrogen and water into ammonia under mild conditions (25°C, 1 atm).[10] This approach addresses two critical challenges: the thermodynamic stability of N_2 and the environmental impact of conventional NH_3 production.[6,7] However, the process must overcome competing hydrogen evolution and low nitrogen solubility in aqueous systems (≈0.6 mM at 25 °C).[10]

Metal–organic frameworks (MOF), particularly zeolitic imidazolate frameworks (ZIFs), have shown exceptional promise as photocatalysts due to their unique structural properties.[11–14] ZIF-8 [Zn(MeIM)$_2$], the most studied variant, combines high surface area (≈1500 m^2 g^{-1}) with molecular sieving capabilities.[15] However, its wide bandgap (4.9–5.2 eV) limits light absorption to the UV region, while rapid charge recombination ($\tau < 1$ ns) reduces photocatalytic efficiency.[16–19] However, strategic metal doping (Co^{2+}, Ni^{2+}, or Fe^{2+} substitution at Zn^{2+} sites) enhances ZIF-8's performance through bandgap narrowing (ΔE_g up to 1.2 eV) and improved N_2 chemisorption.[20,21] These modifications extend light absorption into the visible range while maintaining framework stability.

Plasmonic metal nanoparticles (PMNP) exhibiting localized surface plasmon resonances (LSPRs) have emerged as promising photosensitizers for photocatalytic nitrogen reduction reactions.[15,21–23] Their exceptional light absorption properties, nanoscale light manipulation capabilities, and ability to excite high-energy carriers that can drive redox surface reactions make them effective catalysts for nitrogen-to-ammonia conversion. These plasmonic photocatalysts can extend semiconductor absorption into the visible range. However, they face several challenges, including reduced electron transfer efficiency due to Schottky barriers, physical separation between catalytic centers and LSPR fields, and slow nitrogen dissolution and mass transfer rates.

Herein, we demonstrate that precise structural design of each component is crucial for developing effective PMNP/MOF nanoarchitectures. The core-shell configuration, with AuNPs of controlled morphologies as the core and ZIF-8 or NiZIF-8 as the porous shell, achieves dual functionality: it prevents plasmonic nanoparticle agglomeration while maintaining efficient transport of N_2 molecules and hydrated protons to the AuNP surfaces during illumination. Furthermore, synergistic effects, such as enhanced electron transfer, energy migration, and localized field polarization, collectively promote N_2 activation and stabilize reaction intermediates, leading to substantially improved catalytic performance.

2. Results and Discussion

The plasmonic core-shell nanostructures were synthesized using a two-step method, as schematically illustrated in **Figure 1**. First, gold nanorods (AuNRs) and gold nanostars (AuNSTs) were selected as plasmonic cores due to their asymmetric geometries, which enhance light absorption per nanoparticle compared to other shapes.[24–26] These structures function as nanoantennas and exhibit distinct absorption signatures, making them ideal for this study.[27–29] AuNRs were synthesized using a seed-mediated method, where adjusting the seed quantity enabled precise control over the LSPR, aligning it with the target wavelength in the NIR region (788 nm).[30] The final AuNRs measured 39.7 ± 4.7 nm in length and 10.9 ± 1.2 nm in width (**Figure 2a**; Figure S1a, Supporting Information). Similarly, AuNSTs were synthesized using CTAB as a capping agent, yielding structures with a core diameter of 77.8 ± 19.3 nm and spike lengths of 45.5 ± 19.3 nm (Figure 2b; Figure S1b, Supporting Information) whose optical response was centred at 700 nm due to the tips with a shoulder at 520 nm corresponding to the core (Figure 2c).[22] In the second step, both plasmonic morphologies were individually encapsulated with water-based NiZIF-8 by maintaining the CTAB concentration below the critical micellar concentration (CMC) threshold, ensuring controlled deposition. This approach promoted homogeneous growth, enabled precise modulation of MOF crystal size, and facilitated the preferential adsorption of hydrophobic hydrocarbon chains on the MOF {100} facets.[31] Ultimately, this led to the formation of cubic structures and consistently yielded core-shell colloidal nanocomposites with narrow size distributions (Figure S2, Supporting Information).[32] Additionally, structures without plasmonic compounds (ZIF-8 and NiZIF-8) and Au@ZIF-8 were synthesized as control samples (Figure S3, Supporting Information).

Transmission electron microscopy (TEM) images (Figure 2d–l; Figure S3, Supporting Information) confirm the formation of single-core encapsulation within uniform cubic NiZIF-8 crystals. The elemental distribution within the composite particles was

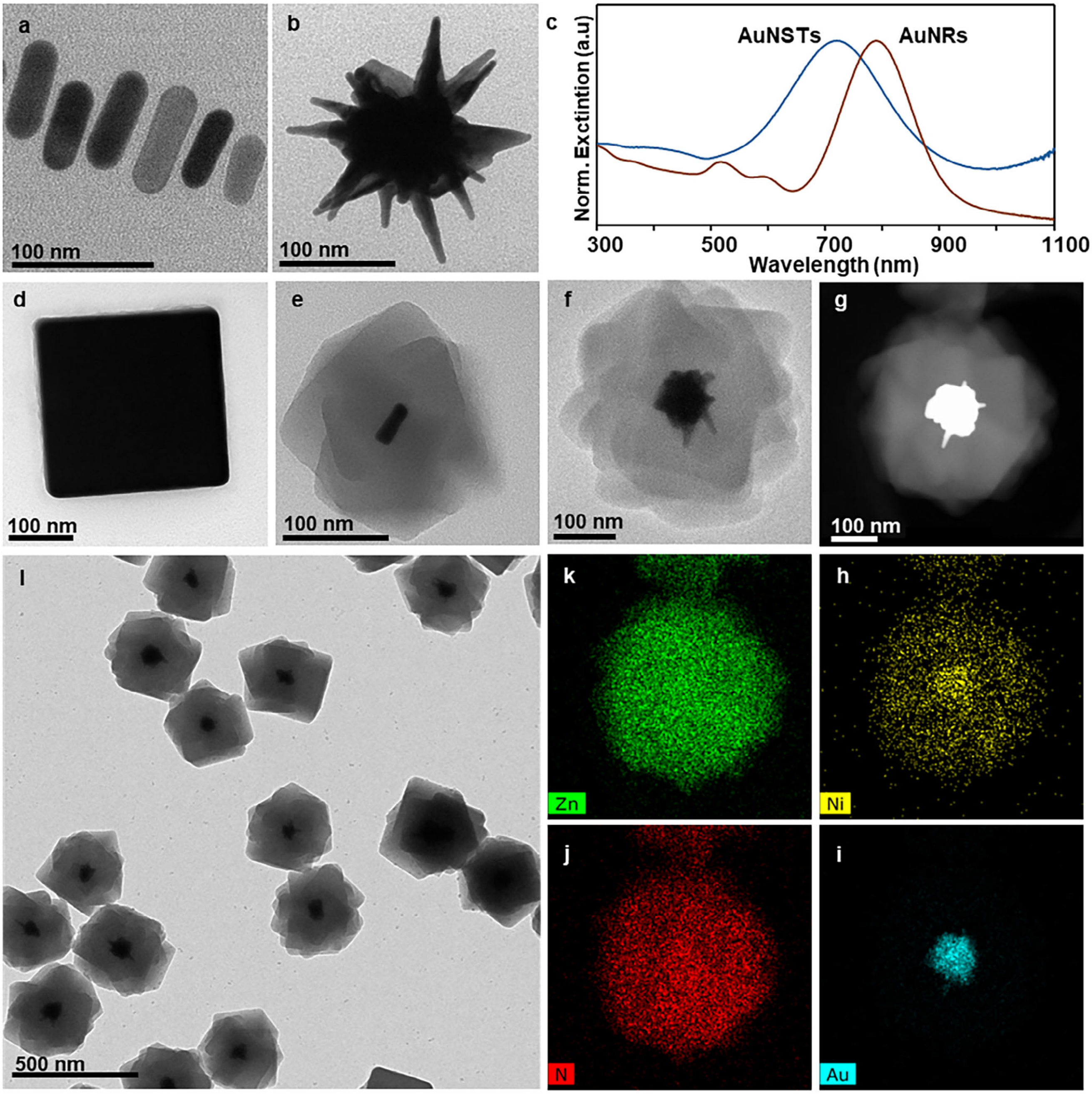

Figure 2. TEM micrograph a) AuNRs, b) AuNSTs, and c) extiction UV–Vis spectra of colloidal AuNRs (Brown) and AuNSTs (blue). High-resolution TEM image d) NiZIF-8 crystal e)AuNR@NiZIF-8, and f) AuNST@NiZIF-8 hybrid, g) the corresponding high-angle annular dark field-scanning transmission electron microscopy (HAADF-STEM) image, h–k) EDX elemental mapping of an Au@NiZIF-8 nanocrystal, l) more representative TEM image of AuNST@NiZIF-8.

confirmed via energy dispersive X-ray spectroscopy (EDX) mapping. As shown in Figure 2h–k, Au was confined to the core, while Zn, N, and Ni were homogeneously distributed throughout the NiZIF-8 shell. Inductively coupled plasma optical emission spectrometry (ICP-OES) results revealed that the Ni loading content of AuNR@NiZIF-8 and AuNST@NiZIF-8 were 1.28 and 1.31 wt.%, respectively.

The comprehensive structural and electronic characterization of Ni-doped and Au-modified ZIF-8 materials reveals a complex but coherent picture of framework modification that maintains crystallinity while introducing strategically important functional properties. Beginning with crystallographic analysis, the powder X-ray diffraction (XRD) patterns (**Figure 3a**) exhibit all characteristic low-angle diffractions of the sodalite-type ZIF-8

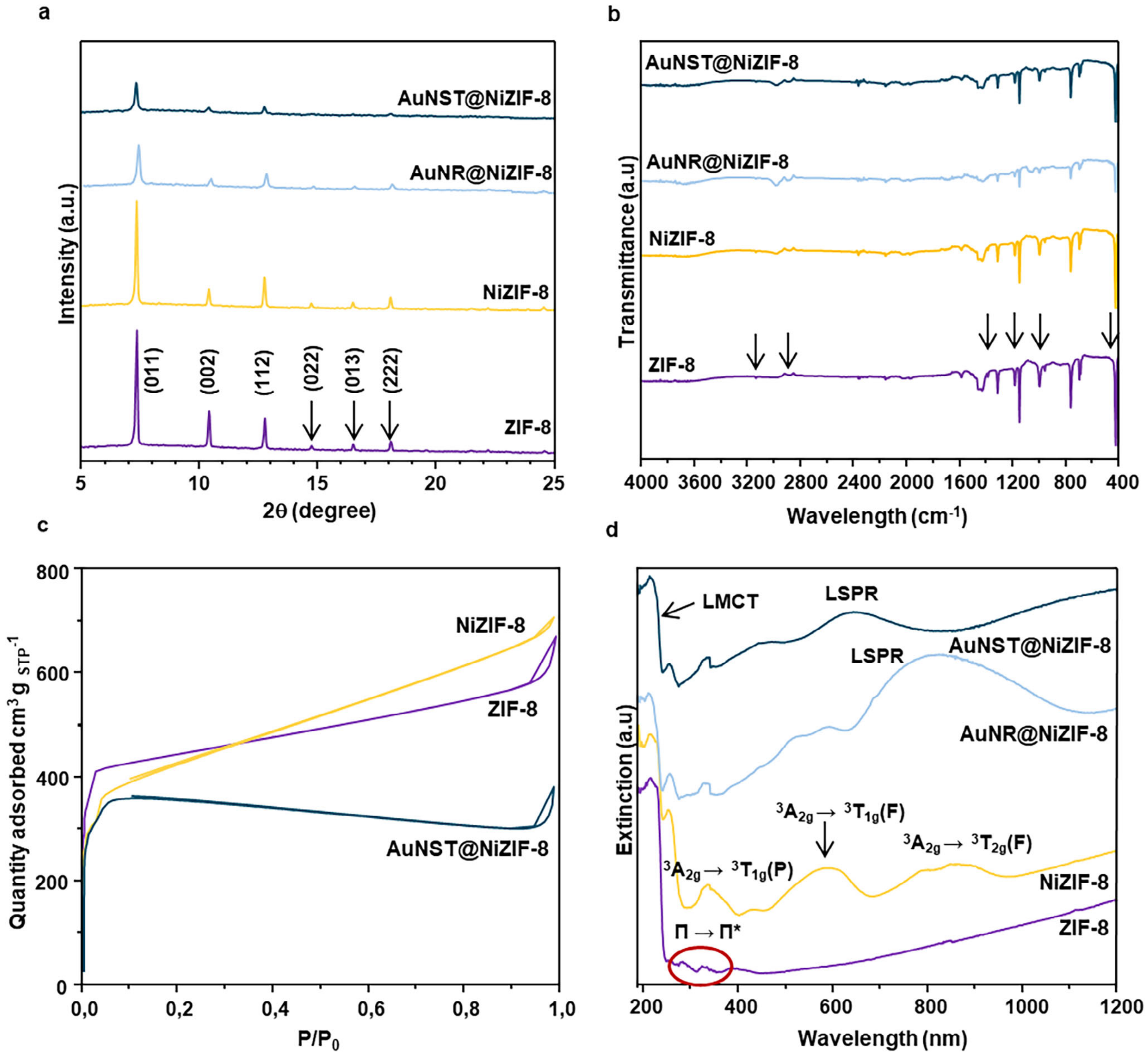

Figure 3. a) Powder XRD profiles and ZIF-8 characteristic peaks, b) FTIR spectra in the zone 4000–400 cm^{-1}, c) N_2 sorption isotherm, and d) Powder UV–Vis DRS. ZIF-8 (purple), NiZIF-8 (yellow), AuNRs@NiZIF-8 (light blue), and AuNSTs@NiZIF-8 (dark blue).

framework, including the prominent (011) reflection at 7.37° (d-spacing = 11.9 Å), (002) at 10.43° ($d = 8.5$ Å), and (112) at 12.78° ($d = 6.9$ Å), with relative intensities matching simulated patterns from single-crystal data.[33] The exceptional peak sharpness (FWHM(011) = 0.12 ± 0.01°) and absence of amorphous halos confirm high crystallinity is maintained after both Ni doping and Au encapsulation. For Au-containing samples, additional reflections at 38.2° (111), 44.4° (200), 64.6° (220), and 77.5° (311) perfectly index to face-centered cubic Au (JCPDS 04-0784), with the (111)/(200) intensity ratio of 3.1 indicating predominantly octahedral (Oh) nanoparticle morphology (Figure S4a, Supporting Information). Notably, the ZIF-8 lattice parameters calculated by Rietveld refinement ($a = 16.991(3)$ Å for ZIF-8 vs. 16.987(5) Å for Ni-ZIF-8) show negligible change, demonstrating that the framework accommodates Ni substitution without significant strain. It should be noted that the crystalline structure remains stable after plasma cleaning and post-catalysis, as demonstrated in Figure S4b (Supporting Information).

Complementary Fourier-transform infrared (FTIR) spectroscopy provides molecular-level resolution of coordination environment changes (Figure 3b). The spectra show all fundamental vibrations of 2-methylimidazolate linkers: aromatic C—H stretching at 3135 cm^{-1} (νas, CH), aliphatic C—H stretching at 2912 cm^{-1} (νs, CH_3), and the intense C═N stretching at 1585 cm^{-1} that serves as a sensitive reporter of metal-ligand bonding.[21] The complete absence of N—H stretching modes in the 1800–1900 cm^{-1} region confirms quantitative deprotonation of the imidazole ligands during synthesis, a prerequisite for proper coordination to metal centers. Most significantly, the metal-nitrogen stretching vibration shifts from 423 cm^{-1} in pristine ZIF-8 to 408 cm^{-1} in Ni-doped samples, a 15 cm^{-1} red shift that directly reflects the changes in metal-ligand bonding upon Ni^{2+} substitution. This shift direction and magnitude agrees perfectly with Badger's rule, given Ni^{2+}'s smaller ionic radius (0.69 Å) compared to Zn^{2+} (0.74 Å), which increases the metal-nitrogen bond strength through greater orbital overlap.[34] The Au-containing samples show no new vibrational modes between 400 and 4000 cm^{-1}, confirming the Au nanoparticles interact through physical dispersion rather than chemical bonding to the framework.

Detailed nitrogen physisorption measurements reveal the hierarchical porosity modifications induced by metal doping and nanoparticle incorporation (Figure 3c). All samples exhibit classical Type I isotherms characteristic of microporous materials, with steep N_2 uptake at low relative pressures ($P/P_n < 0.01$) indicating uniform micropores. The pore size distribution analysis gives an average pore diameter of 1.5 ± 0.1 nm for all samples, matching the theoretical pore opening size in ZIF-8 (Figure S5, Supporting Information). Quantitative analysis shows Ni incorporation reduces the micropore volume from 0.516 $cm^3\ g^{-1}$ (ZIF-8) to 0.319 $cm^3\ g^{-1}$ (NiZIF-8), while maintaining comparable BET surface area (1382 vs 1387 $m^2\ g^{-1}$). This unusual combination, which preserves surface area but reduces pore volume, suggests that Ni^{2+} complexes partially occupy pore cavities without collapsing the framework, consistent with the XRD and FTIR results. For Au-loaded samples, the development of a hysteresis loop at $P/P_n = 0.45–0.90$ indicates new mesoporosity, while the decreased surface area to 1100 $m^2\ g^{-1}$ reflects some degree of physical interaction between the gold nanoparticles and the MOF.

UV–Vis diffuse reflectance spectroscopy (UV–Vis DRS) provides crucial insights into the electronic structure modifications (Figure 3d). Pristine ZIF-8 exhibits only ligand-to-metal charge transfer (LMCT) transitions below 300 nm (imidazolate→Zn^{2+}) due to Zn^{2+}'s d^{10} configuration, which lacks crystal field transitions. In contrast, NiZIF-8 shows three characteristic d-d transitions of Oh Ni^{2+} (d^8): $^3A_2g \rightarrow {}^3T_2g(F)$ at 875 nm (1.42 eV, $\nu1$), $^3A_2g \rightarrow {}^3T_1g(F)$ at 580 nm (2.14 eV, $\nu2$), and $^3A_2g \rightarrow {}^3T_1g(P)$ at 340 nm (3.65 eV, $\nu3$), as predicted by Tanabe-Sugano theory for Oh symmetry.[35] The exceptionally broad bandwidths (FWHM = 2100 ± 150 cm^{-1} for $\nu2$) indicate dynamic Jahn–Teller distortion in the NiN_6 coordination sphere, consistent with the fluxional behaviour of high-spin Ni^{2+} in imidazolate frameworks.[36] For Au-modified samples, plasmonic coupling effects are evident: AuNRs (longitudinal LSPR at 750 nm) show weak interaction with Ni^{2+}'s 875 nm transition, while AuNST (LSPR at 640 nm, blue shifted due to spike reshaping upon ZIF coating) strongly overlap with the 580 nm transition, potentially enabling resonant energy transfer.[37]

X-ray photoelectron spectroscopy (XPS) delivers atomic-level resolution of electronic structure changes (**Figure 4**). The Zn $2p_3/_2$ core level remains remarkably constant at 1021.8 ± 0.1 eV across all samples, with a spin–orbit splitting of 23.1 eV and satellite structure identical to pristine ZIF-8,[38] confirming the framework's electronic resistance to modification. For Ni-doped samples, the Ni $2p_3/_2$ region shows the definitive signature of high-spin Ni^{2+} in Oh coordination: a main peak at 855.7 eV accompanied by charge transfer satellites at 861.9 eV (6.2 eV separation) and 867.3 eV (11.6 eV separation), with intensity ratios matching theoretical predictions for d^8 configuration. Au loading induces a small but reproducible 0.3 eV positive shift in Ni $2p_3/_2$ binding energy (to 856.0 eV), suggesting, very likely, electron withdrawal from Ni centres through Au→Zn→Ni charge transfer pathways mediated by the conjugated imidazolate linkers.[39] While direct operando evidence would be required to unambiguously confirm such a charge-transfer pathway, complementary UV–Vis and wavelength-dependent photocatalysis provide strong support for an Au–Ni electronic interaction. In UV–Vis DRS, the Ni^{2+} d–d transition at ≈580 nm overlaps strongly with the AuNST LSPR (600–700 nm), creating the spectral conditions necessary for plasmonic energy or carrier transfer. Consistently, catalytic action spectra show that restricting illumination to $\lambda > 500$ nm, thus exciting the overlapping Au/Ni window, recovers most of the full-spectrum activity, despite reduced photon flux. Together with the reproducible +0.3 eV Ni $2p_3/_2$ shift, these data support an electronic coupling between Au and Ni that contributes to enhanced photocatalytic activity, although the precise mechanism (near-field enhancement, energy transfer, or hot-carrier injection) remains to be fully resolved. In addition, plasma cleaner treatment applied to the samples effectively cleans the surface without causing significant alterations to their elemental composition or chemical environment. The highly consistent binding energies of the main elements (O, Zn, Ni) clearly confirm the preservation of the overall structural integrity of the material (Table S1, Supporting Information).

Correlating these techniques reveals a sophisticated hierarchical modification mechanism operating across multiple length scales. At the atomic level, Ni^{2+} substitution introduces localized electronic perturbations (XPS shifts, UV–Vis d–d transitions) and bond length changes (FTIR frequency shifts) that subtly alter pore accessibility (physisorption) while maintaining long-range order (XRD). The UV–Vis derived ligand field parameters ($\Delta_n = 11{,}429\ cm^{-1}$ (875 nm)) quantitatively explain both the XPS-observed Ni^{2+} satellite structure and FTIR's Ni-N vibration shift through the nephelauxetic effect. This value, which corresponds to the $^3A_2g \rightarrow {}^3T_2g(F)$ transition observed in the UV–Vis spectrum of Ni^{2+} in octahedral coordination within ZIF-8, confirms the Oh symmetry of the Ni^{2+} sites and aligns with XPS Ni^{2+} oxidation state (855.7 eV), FTIR Ni-N stretching vibration (408 cm^{-1}) and the strain-induced pore volume decrease (0.516 → 0.319 $cm^3\ g^{-1}$). The large Δ_n (11,429 cm^{-1} vs. ≈8,000 cm^{-1} for typical Ni-imidazolates) suggests strong ligand field effects in our system, likely due to framework-induced strain or Au interactions. This high splitting energy stabilizes the low-spin state of Ni^{2+} and enhances back-donation to N_2 in potential ammonia synthesis (nitrogen reduction reaction, NRR) catalysis.

To evaluate the photocatalytic performance of the synthesized samples, we conducted photocatalytic N_2 reduction in a basic aqueous solution under visible light illumination.[40] The ammonia production was quantified by indophenol colorimetric assay and ^1H-NMR spectroscopy.[1] Both techniques showed consistent results, corroborating the measured ammonia yields (Figure S6, Supporting Information). To verify the source of the nitrogen atom in the NH_3 product, isotopic labeling experiments using $^{15}N_2$ were performed. The ^1H NMR spectrum (Figure S7, Supporting Information) exhibits two distinct peaks at 6.89 and 7.08 ppm, corresponding to the $^{15}NH_4{}^+$ species.[41]

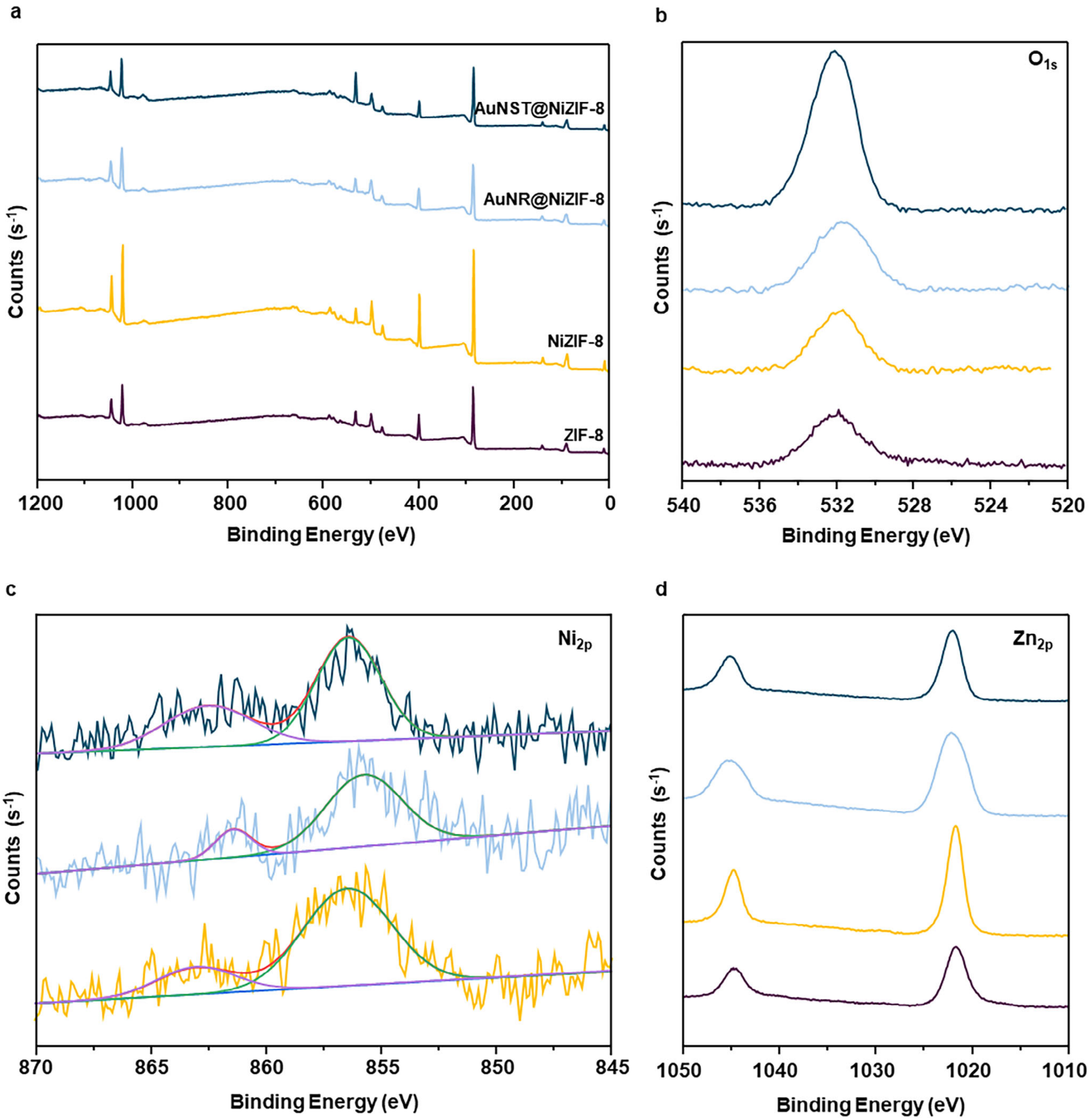

Figure 4. a) XPS survey scans and high-resolution spectra of b) O1s, c) Ni2p, and d) Zn2p of ZIF-8 (purple), NiZIF-8 (yellow), AuNR@NiZIF-8 (light blue), and AuNST@NiZiF-8 (dark blue) hybrids.

Figure 5a illustrates the catalytic performance of the various photocatalysts. Whereas ZIF-8 demonstrated minimal activity, which is consistent with its limited absorption in the visible spectrum, the incorporation of Ni into the framework structure resulted in a fourfold increase in ammonia yield. This improvement can be attributed to the broadening of the light absorption range and the formation of novel energy levels (Figure 3d), which function as both active sites and electron capture centres, thus mitigating charge recombination. Moreover, the integration of Au nanoparticles into the NiZIF-8 framework led to a substantial enhancement in catalytic performance, with a twofold increase for AuNRs and a sevenfold increase for AuNSTs compared to NiZIF-8. The ammonia evolution rates were 57 and 207 μmol g_{cat}^{-1} h^{-1} for the AuNRs@NiZIF-8 and AuNSTs@NiZIF-8 samples, respectively, with the latter surpassing most of the reported results related to plasmon-assisted photocatalytic N_2 reduction in the absence of hole scavengers (Table S2, Supporting Information). Furthermore, it is important to note that when

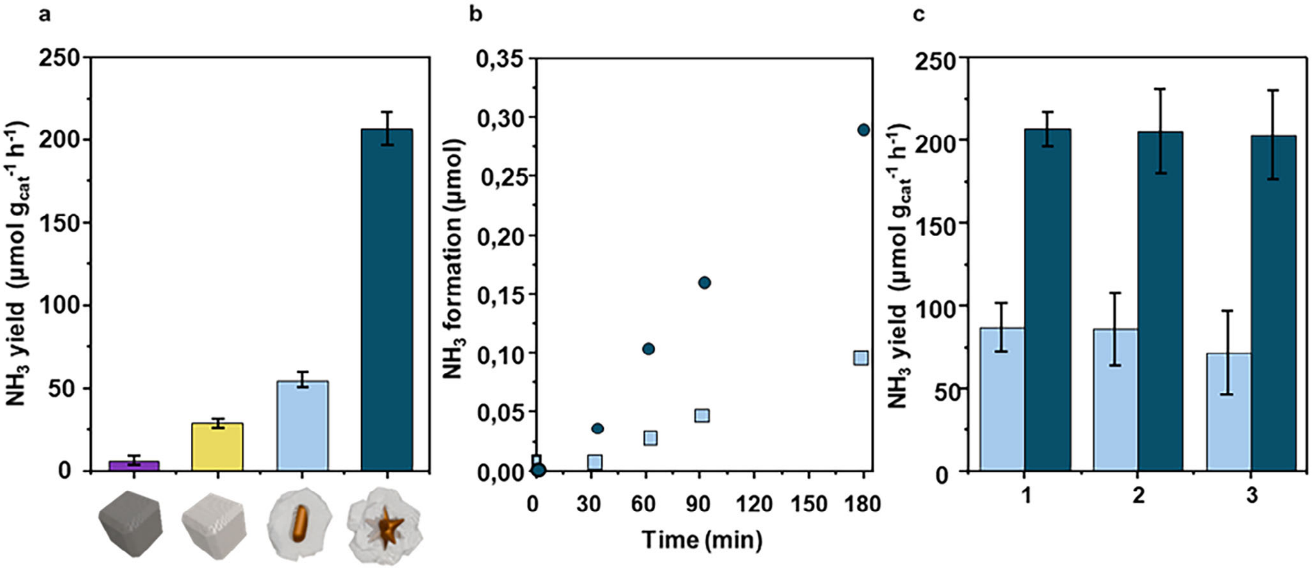

Figure 5. a) NH_3 yield of ZIF-8, NiZIF-8, AuNR@NiZIF-8, and AuNST@NiZIF-8 hybrids under N_2 conditions, with the contribution from Ar subtracted, b) Time evolution of the NH_3 formation using AuNST@NiZIF-8 as photocatalyst, c) NH_3 yield upon 3 consecutive photocatalytic cycles for the AuNR@NiZIF-8, and AuNST@NiZIF-8 samples. Reaction conditions: $m_{cat} = 0.5$ mg, $V_{reactor} = 3$ mL, T = 20°C, t = 1 h per cycle. Wavelength range = 350-2400 nm.

photocatalysis was performed using a mixture of AuNSTs and NiZIF-8, at concentrations comparable to those in the hybrid nanostructure, the ammonia production rate was approximately twofolds lower than that observed with the hybrid system (Figure S8, Supporting Information).

It is also noteworthy that although the performance evaluation of the samples under dark an Ar (Figure S8, Supporting Information) atmosphere demonstrates a certain catalytic activity attributed to the nitrogen group of the methylimidazole ligand, a significant increase in activity is observed when the reaction is conducted under light and N_2. This confirms that the ammonia produced primarily originates from N_2 reduction in the visible region of the solar spectrum. Furthermore, the presence of secondary products, such as hydrogen (H_2) (Figure S9, Supporting Information) and hydrazine (N_2H_4) was assessed by gas chromatography and Watt and Chrisp method (Figure S10, Supporting Information), respectively, and negligible amounts were detected.[42] Figure 5b shows the time evolution of the reaction, with reaction rates of 0.03 µmol h^{-1} and 0.10 µmol h^{-1} for the AuNRs@NiZIF-8 and AuNSTs@NiZIF-8 samples, respectively. The corresponding turnover numbers (TON), calculated per Ni site after 3 h of reaction under solar-simulator irradiation, are ≈234 and 1275, respectively. The stability assessment of the AuNRs@NiZIF-8 and AuNSTs@NiZIF-8 samples demonstrated that its catalytic activity is preserved across 3 consecutive cycles (Figure 5c). Consistent with this, TEM micrographs revealed that the morphology of the nanostructures remains unchanged (Figure S11, Supporting Information) and thereby further confirming the stability of both hybrid structures. Moreover, XRD analysis showed that the crystallinity of the photocatalyst is also preserved as it can be seen in Figure S4b (Supporting Information).

We complement these observations with computational results simulating the optical and photocatalytic response of the AuNPs that were later encapsulated inside the NiZIF-8. Description of the computational details can be found in the Supporting Information,[43,44] and selected results of these simulations are shown in **Figure 6**. From them, it is apparent that the AuNSTs interact much more strongly with light than the AuNRs. This is also true when we evaluate the total rate of excitation of intraband electrons and holes with large excess energies, $Rate_{\mathrm{HE,he}}$, shown in Figure 6b.[44,45] Each AuNST achieves larger rates and also covers a broader spectral range. In the context of the reduction of N_2, the production of these high-energy carriers is particularly relevant, as they can be injected into the environment the metal, and contribute to both reduction of N_2 and creation of required radical species through oxidation. The large excitation rate of such charge carriers in the AuNST occurs preferentially at the tips of its spikes or arms, which are points of large curvature and thus produce strong hot spots, alike those produced at the tips of AuNRs excited at resonance. The surface maps showing the order of magnitude of the field enhancement, in Figure 6c, help us in visualizing them, as well as understanding the geometry of the plasmonic modes excited at the main plasmonic resonance nearest the visible range. For the AuNR, we are of course seeing its longitudinal mode while, less obviously, for the AuNST we find that at 726 nm we are seeing single-spike modes, with the collective mode being present at ≈1200 nm. Incidentally, these surface maps also inform us about the overall spatial distribution of the spots around which the AuNST can induce resonant energy transfer to Ni optical bands, occurring at the wavelengths listed in a previous paragraph.

To examine the wavelength dependence of photocatalytic NRR, experiments were performed using optical filters, and the results are presented in **Figure 7a**. When the hybrid catalyst AuNST@NiZiF-8 was irradiated with light in the 360–517 nm range, gold interband transitions were predominantly excited, resulting in NH_3 production of 39 µmol $g_{cat}{}^{-1}$ h^{-1}. However, when

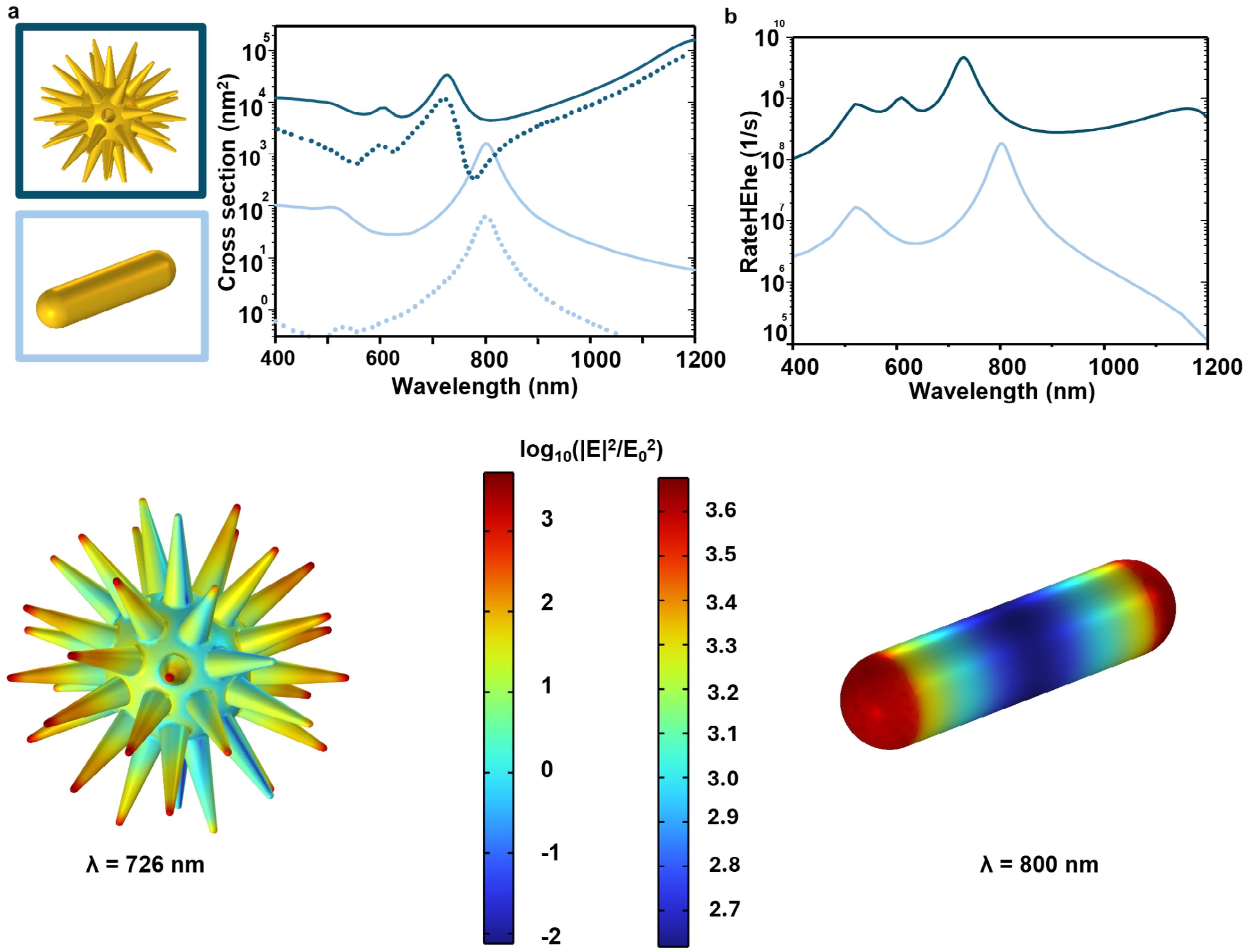

Figure 6. a) Computational scattering (dotted lines) and extinction cross sections (solid lines) of the AuNPs, accompanied by models used in the electromagnetic simulations of both AuNSTs and AuNRs. b) Spectra of the rate of excitation of high-energy intraband carriers for both systems. c) Surface maps of the field enhancement immediately outside of the AuNPs, under excitation with linearly polarized light, aligned with the long axis in the case of the AuNR, at wavelengths of 726 and 800 nm for AuNSTs and AuNRs, respectively.

the irradiation wavelength exceeded 500 nm, so that the excitation included not only the LSPR of AuNSTs but also selectively activated the d–d transitions of Ni in an Oh configuration the result of NH_3 production reached a value close to that obtained with the wider spectral range, from 350 nm wavelength, with 196 μmol g_{cat}^{-1} h^{-1}.[46,47] Considering a 10% transmittance loss due to the use of the optical filter in the 500–2400 nm range (Figure S12, Supporting Information), these results suggest that the most relevant contribution to the catalytic performance of these structures arises from the interaction between the d–d transitions of Ni and the plasmonic component.

To gain deeper insight into the mechanism behind N_2 photoreduction, we conducted control experiments to detect reactive oxygen species (ROS).[48] The primary ROS identified were the hydroxyl radical ($OH^{\cdot}$), formed when H_2O molecules interact with photogenerated holes, as evidenced by the conversion of terephthalic acid (TA) into its fluorescent derivative, 2-hydroxyterephthalic acid (2-HTA) (Figure 7b, Figure S13, Supporting Information). Additionally, we examined the superoxide radical ($O_2^{\cdot-}$), which arises from the reduction of dissolved oxygen by photogenerated electrons, by tracking the transformation of Nitro Blue tetrazolium (NBT) into its formazan form (Figure 7c; Figure S14, Supporting Information). Our results confirmed the presence of both species under photocatalytic conditions in an O_2 and N_2 atmosphere, exhibiting the same trend. This suggests that, regardless of the gas environment, the electrons photogenerated from AuNSTs were injected into the d–d transitions of Ni and subsequently used for N_2 reduction to NH_3. Meanwhile, $OH^{\cdot}$ radicals likely formed either through the interaction of hot holes with water molecules or via the decomposition of photogenerated H_2O_2.[49]

Finally, **Figure 8** provides a graphical representation of our proposed breakdown of the mechanistic contributions to the reaction. The band structures, including higher binding energy (BEH) and lower binding energy (BEL), were estimated from the intersections in Figure S14 (Supporting Information). The valence band potentials (EVB) and conduction band potentials (ECB) were obtained from UV photoelectron spectroscopy (UPS)

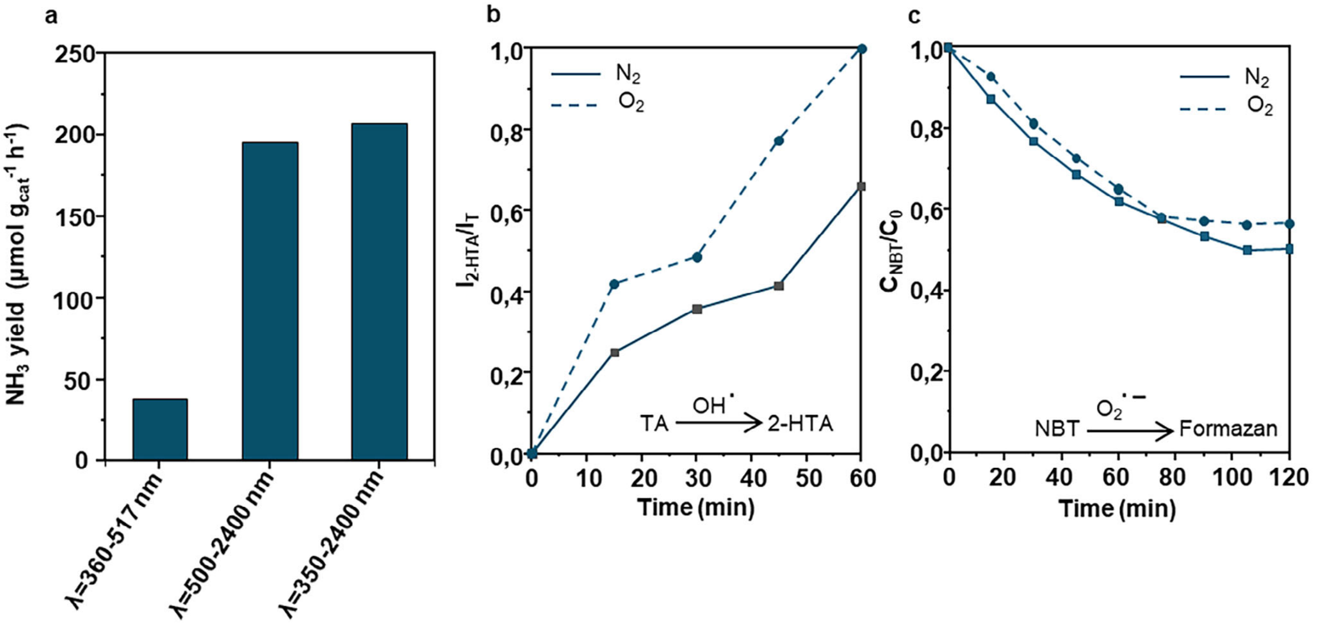

Figure 7. a) Photocatalytic results of the AuNST@NiZIF-8 hybrid obtained upon irradiation in different regions of the solar spectrum. Reaction conditions: m_{cat} = 0.5 mg, $V_{reactor}$ = 3 mL, T = 20°C, t = 1 h. b) Fluorescence spectroscopy detection of $OH^{\cdot}$ through the formation of 2-HTA. c) $O_2^{\cdot -}$ detection through its reaction with NBT using absorption spectroscopy. The solid and dotted lines illustrate the photoreaction of the molecules under N_2 and O_2 atmospheres, respectively, in the presence of the AuNST@NiZIF-8 photocatalyst.

measurements (Figure S15, Supporting Information), while the bandgap energies were calculated by the Tauc plot method. We note, however, that extracting absolute band-edge values from UPS of powders is not without limitations, due to surface contamination (e.g., adventitious carbon), charging effects, and sensitivity to baseline scaling. For this reason, in Figure S15 (Supporting Information) we emphasize only the relative spectral differences among samples, while avoiding over-interpretation of absolute energy positions. Accordingly, UPS is used here qualitatively, supporting the presence of Ni-induced mid-gap states and subtle Au–Ni electronic interactions, while the main mechanistic interpretation relies on the more robust evidence from XPS, UV–Vis DRS, and photocatalytic wavelength-dependence.

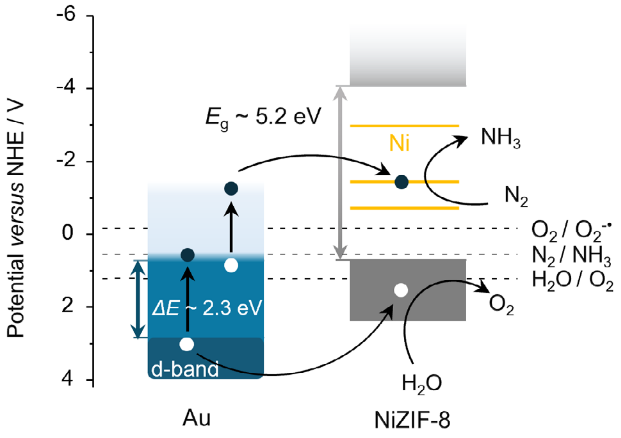

Figure 8. Proposed mechanism for the plasmon-assisted photocatalytic N_2 reduction to NH_3.

Therefore, we propose that two basic mechanisms underlie the photocatalytic improvement when using encapsulated AuNST@NiZIF-8. The first is the straightforward enhancement of Ni absorption, thus improving the efficiency of the metal center catalysts through the nanoantenna effect of the AuNP. The strong hot spots at the tips of the AuNSTs, their large multiplicity, and their better spectral alignment with the 580 nm Ni absorption line, suggest this geometry as a strong candidate for enhancing the promotion of excited states in the Ni. The other mechanism is the injection of both electrons and holes from the metal to the molecular framework, driving the required redox reactions (N_2 reduction and H_2O oxidation, respectively). Given the energy alignment that we expect from the bands of the different materials, as seen in Figure 8, we would expect that the electrons originated in the Au would traverse to nearby orbitals at the Ni atoms, which introduce states within the broad ZIF-8 bandgap. On the other hand, high-energy holes excited in the metal could be expected to traverse into the ZIF-8 valence band, or trigger surface oxidation processes directly on the metal surface.

According to this mechanistic scheme, the system depends on the mid-bandgap states introduced by the Ni in the ZIF-8. These would be populated by the injection of high-energy carriers excited at the surface of the plasmonic nanostructures. See Figure 6b for the simulated spectral response of their excitation rates. The presence of the Ni states within the ZIF-8 bandgap is evidenced by the additional absorption lines present in the NiZIF-8 system, as shown in Figure 3d. To further support their presence, and explore some of its properties, we performed first-principles simulations contrasting pristine ZIF-8 and NiZIF-8. Description of the computational details can be found in the Supporting Information,[50–53] and a summary of the results comparing both systems is presented in **Figure 9**. The single cell for both

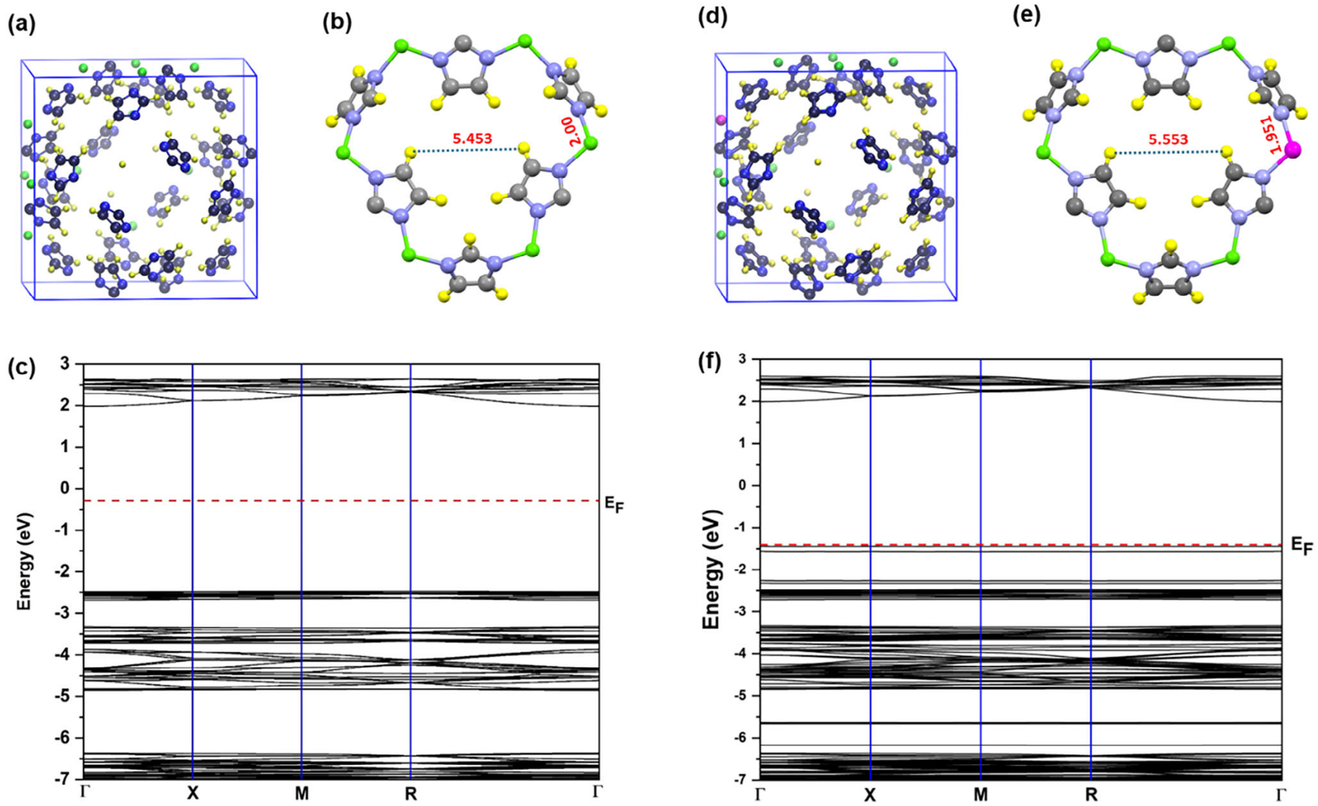

Figure 9. Density Functional Theory results. Optimized atomic structure of the a) ZIF-8 and d) NiZIF-8 unit cell. Herein, Ni, Zn, N, C, and H atoms are represented by magenta, green, blue, black, and yellow spheres, respectively. Supercells with 2 × 2 × 2 unit cells for can be found in Figure S17 (Supporting Information). The local environment of the position hosting the Ni can be seen for the b) pristine ZIF-8 and e) NiZIF-8, showing minor structural modifications due to doping. Electronic band structures for c) pristine ZIF-8 and f) Ni-doped ZIF-8.

systems is presented in Figure 9a,d. The doped system, with a Ni atom substituting a Zn, undergoes minor structural changes, as illustrated by the comparison between Figure 9b,e. The electronic changes, however, are more significant. These can be appreciated in the comparison between Figure 9c,f. We found a bandgap of 4.46 eV for pristine ZIF-8, and an effective reduction of this magnitude upon the introduction of Ni-states in the NiZIF-8 system. The presence of these localized states in the band gap open up new absorption lines in the structure, as seen experimentally, and can also serve as reduction centers, as suggested in Figure 8.

To gain a deeper insight into the electronic structure of the crystal, we mapped key electronic states for both pristine and doped configurations. Figures S18 and S19 (Supporting Information) show the wavefunctions of selected electronic states around the bandgap for pristine ZIF-8 and NiZIF-8 systems, respectively, evaluated at Γ-point. One can see the extended nature of the states corresponding to the valence and conduction band of ZIF-8 and NiZIF-8, and how the states in the bandgap of NiZIF-8 are localized around the Ni atom. In Figure S18 (Supporting Information) (pristine ZIF-8), electronic orbitals in the valence band are evenly delocalized over the π-conjugated organic linkers, indicating strong ligand-centered character. The conduction band orbitals (CB1 and CB2), display a more spatially diffused distribution, extending over both the ligand framework and regions near the metal centers, suggesting a mixed orbital character that may facilitate charge separation. From Figure S19 (Supporting Information), we can see that Ni doping does not lead to notable alterations in the character of these states, but introduces five strongly localized Ni states, three of them close to the Fermi energy. This localization indicates an enhanced metal-centered character, which is absent in the pristine ZIF-8 system at the band edges. Finally, a general point regarding the band structure of both MOFs is the low band dispersion across k-points, which indicates a low charge mobility. This may suggest a relatively local effect of the plasmonic enhancement, be it through charge injection of promoting optical transitions within the MOF.

3. Conclusion

In summary, Au@NiZiF-8 hybrid nanoarchitectures were successfully developed for photocatalytic N_2 reduction to NH_3 using solar light. Among the evaluated morphologies, nanocomposites incorporating AuNST exhibited the highest photocatalytic activity, reaching 206.92 ± 10.3 μmol g_{cat}^{-1} h^{-1}. Moreover, these hybrid nanostructures demonstrated excellent structural stability, maintaining consistent performance over three consecutive cycles. Advanced characterization and computational simulations validated the observed photocatalytic efficiency. Wavelength-dependent studies revealed a synergistic interplay between two key mechanisms. First, the nanoantenna effect of AuNSTs enhances Ni absorption, optimizing metal center efficiency. Second, charge transfer occurs as hot electrons and holes move from Au to Ni d–d transitions in the ZIF-8 framework, facilitating redox reactions and promoting efficient N_2 reduction. Overall, the results of this study emphasize the importance of precise structural design in the development of plasmonic nanoparticles/MOF hybrids, providing a promising pathway for achieving scalable photocatalytic nitrogen reduction.

Supporting Information

Supporting Information is available from the Wiley Online Library or from the author.

Acknowledgements

B.A.-F. and A.M. contributed equally to this work. M.V.-G. and M.A.C.-D. acknowledge financial support from MICIU/AEI/10.13039/501100011033 and FEDER, UE. under project PID2023-147495OB-I00 A.S.C. acknowledges Xunta de Galicia, Spain, for her postdoctoral fellowship. R.A.A.-P. acknowledges financial support from MICIU/AEI/10.13039/501100011033 under projects PID2023-152767NB-I00 and MICIU/AEI/10.13039/501100011033 and FEDER, UE under project PID2020-120306RB-I00. L.V.B. acknowledges support under grant RYC2021-033818-I funded by MICIU/AEI/10.13039/501100011033 and FSE+. M.V.-G. acknowledges financial support from MICIU/AEI/10.13039/501100011033 and FSE+ under grant RYC2022-038390-I and Xunta de Galicia under project ED431F 2025/024. M.V-G and L.V.B acknowledge financial support from MICIU/AEI/10.13039/501100011033 and Unión Europea NextGenerationEU/ PRTR under project TED2021-130038A-I00 This work was carried out in part through the use of the International Iberian Nanotechnology Laboratory (INL) User Facilities. R.K. and L.V.B. acknowledge the Centro de Supercomputación de Galicia (CESGA) for providing computational resources and support. The authors acknowledge the use of scientific and technical services from Centro de Apoio Científico e Tecnolóxico á Investigación (CACTI-Universidade de Vigo). The authors would like to acknowledge Miguel Spuch Calvar for his support with the schemes.

Conflict of Interest

The authors declare no conflict of interest.

Data Availability Statement

The data that support the findings of this study are available from the corresponding author upon reasonable request.

Keywords

gold nanoparticles, hybrid photocatalyst, nitrogen reduction, plasmonic photocatalyst, solar light, ZIF-8 MOF

Received: August 21, 2025
Revised: October 29, 2025
Published online: November 18, 2025

[1] B. Puértolas, M. Comesaña-Hermo, L. V. Besteiro, M. Vázquez-González, M. A. Correa-Duarte, *Adv. Energy Mater.* **2022**, *12*, 2103909.
[2] J. W. Erisman, M. A. Sutton, J. Galloway, Z. Klimont, W. Winiwarter, *Nat. Geosci.* **2008**, *1*, 636.
[3] T. Hu, X. Cheng, J. Luo, Y. Yan, Q. Zhang, Y. Li, *ACS Catal.* **2024**, *14*, 14539.
[4] Y. Feng, L. Jiao, X. Zhuang, Y. Wang, J. Yao, *Adv. Mater.* **2025**, *37*, 2410909.
[5] J. G. Chen, R. M. Crooks, L. C. Seefeldt, K. L. Bren, R. M. Bullock, M. Y. Darensbourg, P. L. Holland, B. Hoffman, M. J. Janik, A. K. Jones, M. G. Kanatzidis, P. King, K. M. Lancaster, S. V. Lymar, P. Pfromm, W. F. Schneider, R. R. Schrock, *Science* **2018**, *360*, aar6611.
[6] X. Han, S. Yang, M. Schröder, *J. Am. Chem. Soc.* **2023**, *145*, 1998.
[7] M. Capdevila-Cortada, *Nat Catal.* **2019**, *2*, 1055.
[8] V. Kyriakou, I. Garagounis, A. Vourros, E. Vasileiou, M. Stoukides, *Joule* **2020**, *4*, 142.
[9] S. Ezendam, M. Herran, L. Nan, C. Gruber, Y. Kang, F. Gröbmeyer, R. Lin, J. Gargiulo, A. Sousa-Castillo, E. Cortés, *ACS Energy Lett.* **2022**, *7*, 778.
[10] D. Ješić, B. Pomeroy, K. M. Kamal, Ž. Kovačič, M. Huš, B. Likozar, *Adv. Energy Sustainability Res.* **2024**, *5*, 2400083.
[11] G. Ren, J. Zhao, Z. Zhao, Z. Li, L. Wang, Z. Zhang, C. Li, X. Meng, *Angew. Chem., Int. Ed.* **2024**, *63*, 202314408.
[12] L. W. Chen, Y. C. Hao, Y. Guo, Q. Zhang, J. Li, W. Y. Gao, L. Ren, X. Su, L. Hu, N. Zhang, S. Li, X. Feng, L. Gu, Y. W. Zhang, A. X. Yin, B. Wang, *J. Am. Chem. Soc.* **2021**, *143*, 5727.
[13] Y. Sun, H. Ji, Y. Sun, G. Zhang, H. Zhou, S. Cao, S. Liu, L. Zhang, W. Li, X. Zhu, H. Pang, *Angew. Chem., Int. Ed.* **2024**, *63*, 202316973.
[14] B. Guo, X. Cheng, Y. Tang, W. Guo, S. Deng, L. Wu, X. Fu, *Angew. Chem., Int. Ed.* **2022**, *61*, 202117244
[15] T. Zorlu, I. B. Becerril-Castro, B. Puertolas, V. Giannini, M. A. Correa-Duarte, R. A. Alvarez-Puebla, *Angew. Chem., Int. Ed.* **2023**, *62*, 202305299.
[16] Y. Yang, G. Tang, X. Liu, Li. Yang, R. Gao, C. P. Li, *Chem. Commun.* **2024**, *60*, 14858.
[17] B. Chen, Z. Yang, Y. Zhu, Y. Xia, *J. Mater. Chem. A* **2014**, *2*, 16811.
[18] L. Chen, Y. Peng, H. Wang, Z. Gu, C. Duan, *Chem. Commun.* **2014**, *50*, 8651.
[19] T. Zorlu, I. B. Becerril-Castro, A. Sousa-Castillo, B. Puértolas, L. V. Besteiro, Z. Wang, A. Govorov, M. A. Correa-Duarte, R. A. Alvarez-Puebla, *Adv. Funct. Mater.* **2024**, *34*, 2410352.
[20] B. Wang, J. Ma, R. Yang, B. Meng, X. Yang, Q. Zhang, B. Zhang, S. Zhuo, *Angew. Chem., Int. Ed.* **2024**, *63*, 202404819.
[21] L. L Zulfa, A. R. P. Hidayat, W. P. Utomo, R. Subagyo, E. N. Kusumawati, Y. Kusumawati, D. Hartanto, W. Widyastuti, R. Ediati, *Case Stud. Chem. Environ. Eng.* **2024**,*10*, 100828.
[22] C. Carrillo-Carrión, R. Martínez, M. F. Navarro Poupard, B. Pelaz, E. Polo, A. Arenas-Vivo, A. Olgiati, P. Taboada, M. G. Soliman, Ú. Catalán, S. Fernández-Castillejo, R. Solà, W. J. Parak, P. Horcajada, R. A. Alvarez-Puebla, P. del Pino, *Angew. Chem., Int. Ed.* **2019**, *58*, 7078.
[23] S. Wang, Y. Fan, J. Teng, Y.-Z. Fan, J.-J. Jiang, H.-P. Wang, H. Grützmacher, D. Wang, C.-Y. Su, *Small* **2016**, *12*, 5702.
[24] A. Sousa-Castillo, M. Comesaña-Hermo, B. Rodríguez-González, M. Pérez-Lorenzo, Z. Wang, X.-T. Kong, A. O. Govorov, M. A. Correa-Duarte, *J. Phys. Chem. C* **2016**, *120*, 11690.
[25] D. B. Ingram, P. Christopher, J. L. Bauer, S. Linic, *ACS Catal.* **2011**, *1*, 1441.
[26] I. B. Becerril-Castro, I. Calderon, N. Pazos-Perez, L. Guerrini, F. Schulz, N. Feliu, I. Chakraborty, V. Giannini, W. J. Parak, R. A. Alvarez-Puebla, *Anal. Sens.* **2022**, *2*, 202200005.
[27] K. Li, N. J. Hogan, M. J. Kale, N. J. Halas, P. Nordlander, P. Christopher, *Nano Lett.* **2017**, *17*, 3710.
[28] K. Trofymchuk, K. Kołątaj, V. Glembockyte, F. Zhu, G. P. Acuna, T. Liedl, P. Tinnefeld, *ACS Nano* **2023**, *17*, 1327.

[29] M. Cedrún-Morales, M. Ceballos, E. Soprano, G. Zampini, E. Polo, B. Pelaz, P. del Pino, *Small Sci.* **2024**, *4*, 2400088.
[30] L. Scarabelli, A. Sánchez-Iglesias, J. Pérez-Juste, L. M. Liz-Marzán, *J. Phys. Chem. Lett.* **2015**, *6*, 4270.
[31] Y. Pan, D. Heryadi, F. Zhou, L. Zhao, G. Lestari, H. Su, Z. Lai, *CrystEngComm* **2011**, *13*, 6937.
[32] G. Zheng, S. de Marchi, V. López-Puente, K. Sentosun, L. Polavarapu, I. Pérez-Juste, E. H. Hill, S. Bals, L. M. L-Marzán, I. Pastoriza-Santos, J. Pérez-Juste, *Small* **2016**, *12*, 3935.
[33] Y. Zhang, Y. Jia, M. Li, L. Hou, *Sci. Rep.* **2018**, *8*, 9597.
[34] R. M. Badger, *J. Chem. Phys.* **1934**, *2*, 128.
[35] Y. Tanabe, S. Sugano, *J. Phys. Soc. Jpn.* **1954**, *9*, 766.
[36] H. A. Jahn, E. Teller, *Proc. R. Soc. A* **1937**, *161*, 220.
[37] L. Rodríguez-Lorenzo, J. M. Romo-Herrera, J. Pérez-Juste, R. A. Alvarez-Puebla, L. M. Liz-Marzán, *J. Mater. Chem.* **2011**, *21*, 11544.
[38] S. K. Sharma, K. Sudarshan, A. K. Yadav, S. N. Jha, D. Bhattacharyya, P. K. Pujari, *J. Phys. Chem. C* **2019**, *123*, 22273.
[39] F. Hillman, H.-K. Jeong, *ACS Appl. Mater. Interfaces* **2019**, *11*, 18377.
[40] Y. Zhao, R. Shi, X. Bian, C. Zhou, Y. Zhao, S. Zhang, F. Wu, G. I. N. Waterhouse, L.-Z. Wu, C.-H. Tung, T. Zhang, *Adv. Sci.* **2019**, *6*, 1802109.
[41] X. Peng, Y. Mi, H. Bao, Y. Liu, D. Qi, Y. Qiu, L. Zhuo, S. Zhao, J. Sun, X. Tang, J. Luo, X. Liu, *Nano Energy* **2020**, *78*, 105321.
[42] G. W. Watt, J. D. Chrisp, *Anal. Chem.* **1952**, *24*, 2006.
[43] P. B. Johnson, R. W. Christy, *Phys. Rev. B* **1972**, *6*, 4370.
[44] L. V. Besteiro, X.-T. Kong, Z. Wang, G. Hartland, A. O. Govorov, *ACS Photonics* **2017**, *4*, 2759.
[45] E. Y. Santiago, L. V. Besteiro, X.-T. Kong, M. A. Correa-Duarte, Z. Wang, A. O. Govorov, *ACS Photonics* **2020**, *7*, 2807.
[46] T.-C. Hung, Y. Godinez-Loyola, M. Steinbrecher, B. Kiraly, A. A. Khajetoorians, N. L. Doltsinis, C. A. Strassert, D. Wegner, *J. Am.Chem. Soc.* **2024**, *146*, 8858.
[47] S. I. Ting, S. Garakyaraghi, C. M. Taliaferro, B. J. Shields, G. D. Scholes, F. N. Castellano, A. G. Doyle, *J. Am. Chem. Soc.* **2020**,*142*, 5800.
[48] J. Q. Wang, S. P. Teong, S. N. Riduan, A. Armugam, H. F. Lu, S. J. Gao, Y. K. Yean, J. Y. Ying, Y. G. Zhang, *J. Am.Chem. Soc.* **2024**, *146*, 599.
[49] G. Yi, X. Li, Y. Yuan, Y. Zhang, *Environ. Sci.: Nano* **2019**, *6*, 68.
[50] P. Giannozzi, S. Baroni, N. Bonini, M. Calandra, R. Car, D. Ceresoli, C. Cavazzoni, G. L. Chiarotti, M. Cococcioni, I. Dabo, A. Dal Corso, S. de Gironcoli, S. Fabris, G. Fratesi, R. Gebauer, U. Gerstmann, C. Gougoussis, A. Kokalj, M. Lazzeri, L. Martin-Samos, N. Marzari, F. Mauri, R. Mazzarello, S. Paolini, L. Paulatto, A. Pasquarello, C. Sbraccia, S. Scandolo, G. Sclauzero, A. P. Seitsonen, et al., *J. Phys.: Condens. Matter* **2009**, *21*, 395502.
[51] J. P. Perdew, K. Burke, M. Ernzerhof, *Phys. Rev. Lett.* **1996**, *77*, 3865.
[52] H. J. Monkhorst, J. D. Pack, *Phys. Rev. B* **1976**, *13*, 5188.
[53] O. Karagiaridi, M. B. Lalonde, W. Bury, A. A. Sarjeant, O. K. Farha, J. T. Hupp, *J. Am. Chem. Soc.* **2012**, *134*, 18790.